

Article

Ultraviolet-C Photoresponsivity Using Fabricated TiO₂ Thin Films and Transimpedance-Amplifier-Based Test Setup

Marilou Cadatal-Raduban^{1,2,*} , Jade Pope¹, Jiří Olejníček³, Michal Kohout³, John A. Harrison¹ 
and S. M. Rezaul Hasan^{4,*}

¹ School of Natural Sciences, Massey University, Auckland 0632, New Zealand

² Institute of Laser Engineering, Osaka University, 2-6 Yamadaoka, Suita 565-0871, Osaka, Japan

³ Department of Low Temperature Plasma, Institute of Physics of the Czech Academy of Sciences, Na Slovance 1999/2, 182 21 Prague 8, Czech Republic

⁴ Center for Research in Analog and VLSI Microsystem Design, Massey University, Auckland 0632, New Zealand

* Correspondence: m.raduban@massey.ac.nz (M.C.-R.); hasanmic@massey.ac.nz (S.M.R.H.)

Abstract: We report on fabricated titanium dioxide (TiO₂) thin films along with a transimpedance amplifier (TIA) test setup as a photoconductivity detector (sensor) in the ultraviolet-C (UV-C) wavelength region, particularly at 260 nm. TiO₂ thin films deposited on high-resistivity undoped silicon-substrate at thicknesses of 100, 500, and 1000 nm exhibited photoresponsivities of 81.6, 55.6, and 19.6 mA/W, respectively, at 30 V bias voltage. Despite improvements in the crystallinity of the thicker films, the decrease in photocurrent, photoconductivity, photoconductance, and photoresponsivity in thicker films is attributed to an increased number of defects. Varying the thickness of the film can, however, be leveraged to control the wavelength response of the detector. Future development of a chip-based portable UV-C detector using TiO₂ thin films will open new opportunities for a wide range of applications.

Keywords: titanium dioxide; thin film; ultraviolet; UV-C; photoconductive detector; sensor; transimpedance amplifier



Citation: Cadatal-Raduban, M.; Pope, J.; Olejníček, J.; Kohout, M.; Harrison, J.A.; Hasan, S.M.R. Ultraviolet-C Photoresponsivity Using Fabricated TiO₂ Thin Films and Transimpedance-Amplifier-Based Test Setup. *Sensors* **2022**, *22*, 8176. <https://doi.org/10.3390/s22218176>

Academic Editors: Maria Leilani Torres, Anna Chiara De Luca and Areti Mourka

Received: 19 September 2022

Accepted: 19 October 2022

Published: 25 October 2022

Publisher's Note: MDPI stays neutral with regard to jurisdictional claims in published maps and institutional affiliations.



Copyright: © 2022 by the authors. Licensee MDPI, Basel, Switzerland. This article is an open access article distributed under the terms and conditions of the Creative Commons Attribution (CC BY) license (<https://creativecommons.org/licenses/by/4.0/>).

1. Introduction

Ultraviolet radiation (UV), broadly used to refer to the wavelength range from 100 nm to 400 nm, has widespread and important scientific, industrial, and medical applications including spectroscopy, photochemical processing, disinfection, and sterilization. UV-C (100–280 nm wavelength) provides an environmentally friendly and chemical-free means for sterilization because of its germicidal effects on a broad spectrum of microorganisms [1–5]. The detrimental effect to the microbial cells is due to the critical damage inflicted to the microbes' genetic material (RNA, DNA, and proteins) by the absorbed UV-C photons. The micro-organism is most vulnerable to photons with a 260 nm wavelength, where the relative susceptibility of RNA and DNA also peaks [6]. Recent works have particularly shown the efficacy of UV-C in completely inactivating corona viruses, including SARS-CoV-2, on surfaces or aerosols [7–10]. Research on portable light sources emitting UV-C wavelengths has seen tremendous growth, especially due to demands for sterilizing surfaces [11,12]. It is expected that development of portable UV-C detectors would follow suit.

Photoconductive detectors made with semiconductors are most promising for developing portable chip-based detectors because of their efficiency, reliability, and simplicity [13]. The wavelength detection limit of such detectors is dictated by the band gap of the semiconductor material, without having to use optical filters. Furthermore, the band gap can be tuned by controlling the composition ratio [14] and the fabrication parameters [15,16]. Zinc oxide (ZnO) [17], gallium nitride (GaN) [18], aluminum nitride (AlN) [19,20], and

boron nitride (BN) [21–25] are semiconductor materials that have been reported as UV photoconductive detectors, each with their own advantages and disadvantages. Diamond has also been reported for UV detection, however, it is a less attractive option due to the high production cost and requirement for low defect concentration as well as the difficulty of incorporating n-type and p-type dopants [26–28]. Additionally, the band gap of diamond is not tunable. In this paper, we explore the photoconductivity of titanium dioxide (TiO₂) thin films in the UV-C wavelength region, especially with 260 nm wavelength excitation. Mostly known for its UV photocatalytic activity, TiO₂ has excellent chemical, physical, and optical properties including being a wide band-gap semiconductor [29,30]. Compared with ZnO, GaN, AlN, and BN, TiO₂ is relatively easier and cheaper to fabricate. The wide band gap of TiO₂ allows detection of UV-C radiation without having to use filters to block out unwanted visible radiation. In conjunction with the UV-C thin-film photoconductive material, a chip-based readout would be necessary when developing a portable detector. Previously, we have reported a Floating Gate Radiation Field Effect Transistor (FGRADFET) sensor, which is a single-chip implementation employing standard single-poly 130 nm CMOS technology [13]. Although the implementation of such a sensor was successful in determining the absorbed dose and dose rate with X-ray excitation, the photoactive material cannot be readily changed from what is commercially available because of the nanometer-sized structure of the channel and gates. In this work, the photoconductivity of TiO₂ thin-film layers deposited on a high-resistivity undoped silicon (Si) substrate was measured in conjunction with a custom-designed transimpedance amplifier (TIA) chip for future development of a chip-based portable UV-C detector. The effect of film thickness on the photoconductivity of TiO₂ thin films deposited on the Si substrate is also investigated for the first time. Our results show that the increasing number of defects in thicker films will be an important consideration when developing a portable photoconductive detector for sensing high-energy radiation such as X-rays, where the high penetration depth would require film thicknesses of a few tens of micrometers.

2. Materials and Methods

2.1. Preparation of TiO₂ Thin-Film Photoconductive Detector

Reactive direct current (DC) magnetron sputtering was used to fabricate the TiO₂ thin films. Before deposition, the deposition chamber was evacuated to 1×10^{-3} Pa base pressure. A pure titanium (99.995% purity) target was used to sputter the films onto a high-resistivity undoped Si substrate. The target has a diameter of 6 inches (15 cm). The Si substrate has a thickness of 0.80 mm, resistivity of 1 k Ω ·cm, and an orientation in the (1 0 0) plane. The films were sputtered in reactive oxygen (O₂) and argon (Ar) atmosphere, maintaining an O₂: Ar gas mixture ratio of 1:4. This ratio was achieved by keeping a constant flow rate of 5 sccm for O₂ and 20 sccm for Ar. The total gas pressure was controlled at 1.3 Pa during deposition. A deposition rate of 5 nm/min was achieved by using a power density of 3.4 W/cm², corresponding to an absorbed power of 600 W. To evaluate the effect of thickness on photoconductivity, films with a thickness of 100 nm, 500 nm, and 1000 nm were fabricated. The desired thickness of the deposited film was obtained by adjusting the deposition time. The thickness of the films was also confirmed after deposition using a surface profilometer with an accuracy error under $\pm 10\%$. To obtain crystalline TiO₂ with good stoichiometry, the deposited films were annealed at 450 C in air for 8 h. A pair of interdigitated electrodes were then deposited on the surface of the films to fabricate the photoconductive detector shown in Figure 1a. A pure Al (99.99%) target was used to deposit the electrodes through a stainless-steel mask using the same chamber used in depositing the TiO₂ films. Deposition of the electrode was carried out in Ar atmosphere with an Ar flow rate of 20 sccm and a working pressure of 1 Pa. The length of the electrode is 7.8 mm, and the distance between the electrode pair is 0.2 mm, giving a sensing area of about 75 mm². The thickness of the electrode is 500 nm.

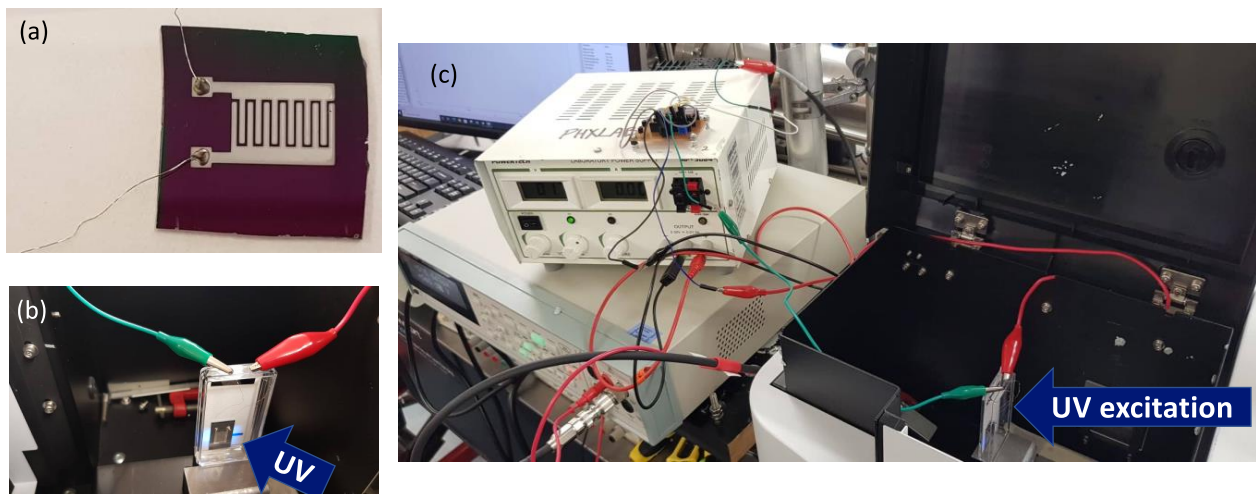


Figure 1. (a) Photograph of the TiO₂ thin-film photoconductive detector. (b) Photograph of the detector being illuminated by 260 nm UV-C radiation. (c) Photograph of the experimental setup used to measure the photoconductivity of the detectors.

2.2. Characterization of the Structural and Optical Properties of the TiO₂ Thin Films

An Empyrean X-ray diffractometer (XRD) fitted with a Cu K α source emitting at a wavelength of 0.154 nm was used to evaluate the crystallinity, strain, and crystallite or particle size of the TiO₂ films. The X-ray diffractometer was operated in grazing incidence geometry with a 2θ range of 10 to 90 and a step size of 0.01. The diffraction patterns were analyzed qualitatively using a HighScore Plus 4.0 software package to obtain the peak positions and their corresponding full-width at half-maximum (FWHM) broadening. The strain and the crystallite size for each film was obtained using the Williamson–Hall plot method, whereby the total broadening (FWHM) observed in the XRD spectrum is a combination of the broadening due to the crystallite size (β_D) and due to the strain (β_ϵ) according to Equations (1) and (2):

$$\beta_D = \frac{K\lambda}{D \cos \theta} \quad (1)$$

also known as the Scherrer formula, where β_D is the FWHM broadening due to the crystallite size, K is the shape factor that is equal to 0.9, λ is the wavelength of the X-ray source, which is 0.154 nm, D is the crystallite size, and θ is the peak position in radians.

$$\beta_\epsilon = 4\epsilon \tan \theta \quad (2)$$

where β_ϵ is the FWHM broadening due to strain, ϵ is the strain, and θ is the peak position in radians.

By deconvolving the XRD spectrum into the amorphous phase contribution (broad curves) and crystalline contribution (sharp diffraction peaks) and integrating each of these contributions, the degree of crystallinity for each film can be calculated from the ratio of the crystalline contribution (A_c) to the amorphous contribution (A_a) according to

$$\text{crystallinity} = \frac{A_c}{A_c + A_a} \times 100 \quad (3)$$

The optical properties of the TiO₂ films were evaluated using their transmission spectra from 200 nm to 700 nm, which were obtained using a double-beam UV-visible near-infrared spectrophotometer. Since Si is opaque to optical wavelengths, identical films were fabricated on a highly transmitting quartz glass substrate. The deposition of the films on quartz glass were carried out at the same time as the films on Si to ensure the same deposition parameters and thickness. The photoluminescence emission spectra of the

films were obtained using a spectrofluorophotometer fitted with a 150 W xenon lamp. The 260 nm UV-C excitation wavelength was selected by a monochromator and was incident on the surface of the TiO_2 film. Photoluminescence emission spectra from the thin film were measured by scanning the grating of the emission spectrometer after passing through a 280 nm high-pass optical filter. The photomultiplier tube (PMT) output signal was corrected for the variation in wavelength sensitivity of the instrument.

2.3. Transimpedance Amplifier-Based Test Setup and Evaluation of Photoconductivity of the TiO_2 Detectors

The photoconductivity of the thin-film photodetector was evaluated using a transimpedance amplifier (TIA)-based test setup. The circuit diagram of the TIA test setup and the photograph of the test board with the TIA chip are shown in the Figure 2a,b, respectively. The breakdown voltage of the discrete bipolar transistor (BC337) used for the current mirror devices Q1 and Q2 is about 45 V, which defines the maximum bias voltage applied to the detector. Therefore, in measuring the dark currents and the photocurrents, a bias voltage of up to 40 V was applied to the TiO_2 detector. A VDD of 1.8 V was applied to the TIA chip. The resistance of the potentiometer was set to 100 Ω . The chip output and input is biased at 0.9 V. The bias voltage of 0.9 V at the collector of Q2 (TIA input) and the diode connection of Q1 ensures that both Q1 and Q2 operate in the forward-active region, and the current mirror functions accurately. The TIA chip was designed in-house and fabricated through the TSMC 180 nm CMOS Foundry. The TIA has a g_m -boosted inverter configuration with resistor feedback biasing provided by R_F .

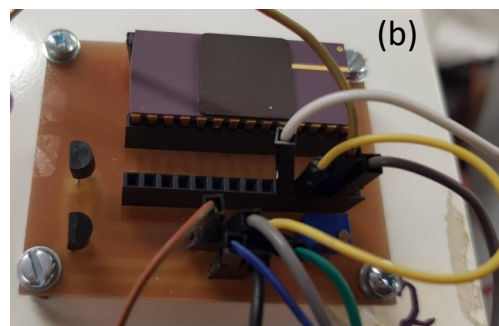
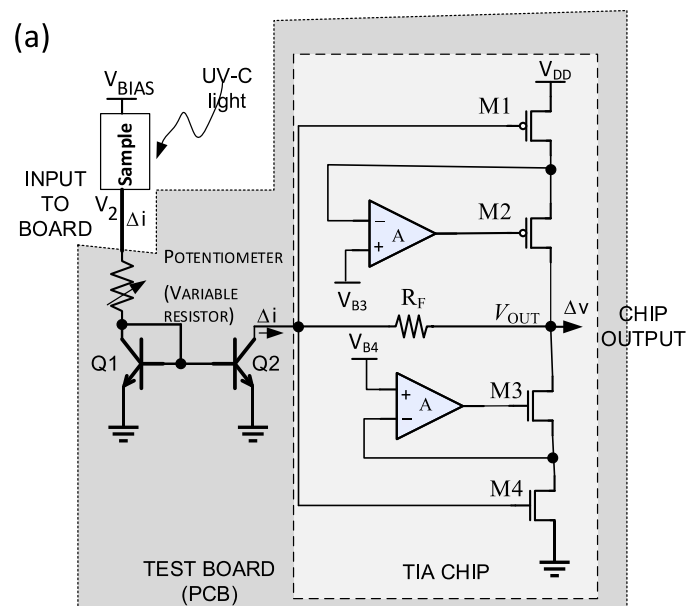


Figure 2. (a) Schematic diagram of the TIA chip and test board setup and (b) photograph of the fabricated test board with TIA chip.

The sensing area of the thin-film detector was illuminated with the 260 nm UV-C emission of a xenon lamp, as shown in Figure 1b. A bias voltage of up to 40 V was applied to one of the aluminum electrodes, and the other electrode was connected to the potentiometer at the test board input as shown in the Figure 2a. As a result, the photo-generated carriers created a drift current due to the applied electric field. A photocurrent was thus generated that is fed to the transimpedance amplifier through the current mirror formed by Q1 and Q2. The output from the TIA was measured using an ultra-high-resistance electrometer. The equipment set-up is shown in the Figure 1c. The dark current was measured using the same measurement setup, except that the detector was kept in the dark by turning off the xenon lamp. The wavelength response of the titanium-dioxide detectors was evaluated by tuning the excitation wavelength from 200 nm to 400 nm, while a 40 V bias voltage is applied to the detector. Since the monochromator's efficiency and the lamp's emissivity changes over this wavelength range; the measured photocurrents were corrected for the wavelength dependence of the excitation source.

3. Results and Discussion

Figure 3 shows the XRD spectra of the TiO₂ films with a thickness of 100 nm, 500 nm, and 1000 nm. All the diffraction peaks observed can be assigned to the anatase phase of TiO₂. The films have a preferred grain orientation in the (0 0 4) direction at 37.8. While all the films are crystalline, the degree of crystallinity improved from 50% to 81% as the thickness increased. The crystallite size likewise increased from 9.6 nm to 26.6 nm as the thickness increased. On the other hand, the strain decreased from 2.4×10^{-3} to 5.2×10^{-5} as the thickness increased. These results are summarized in Table 1.

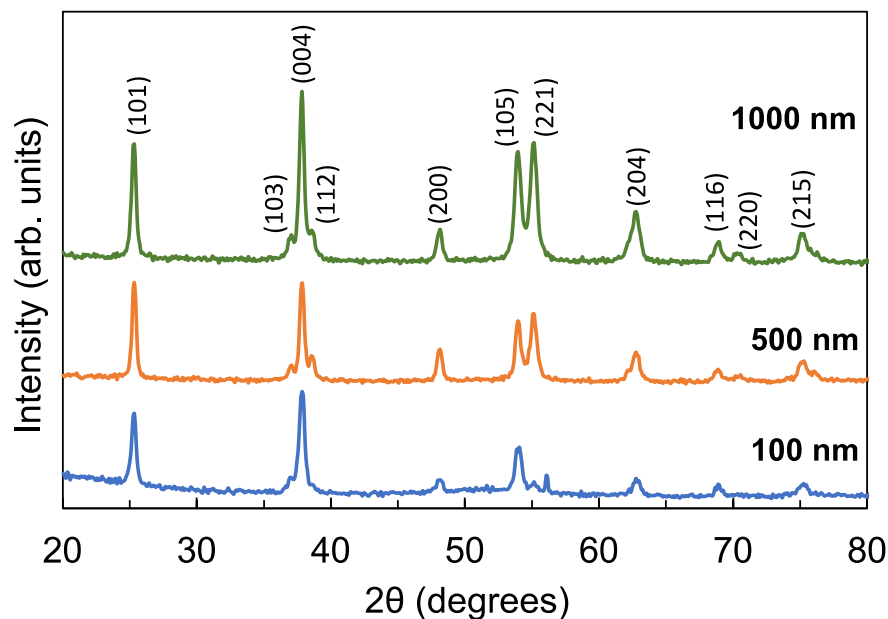


Figure 3. XRD spectra of the TiO₂ films with film thicknesses of 100 nm, 500 nm, and 1000 nm. All peaks are indexed to the anatase phase of TiO₂.

Table 1. Strain, crystallite size, and crystallinity of the TiO₂ films with 100 nm, 500 nm, and 1000 nm film thicknesses.

Thickness (nm)	Strain	Crystallite Size (nm)	Crystallinity (%)
100	2.4×10^{-3}	9.6	50
500	4.5×10^{-3}	23.5	78
1000	5.2×10^{-3}	26.6	81

The transmission and absorption spectra of the films are shown in Figure 4a,b, respectively. The transmission spectra of the films on the substrate were divided by the transmission spectrum of a reference substrate to exclude the contribution of the substrate. The sinusoidal fluctuations in the transmittance curves are Fabry–Perot interference fringes. The films have similar transmittances at the long-wavelength region, but a significant decrease in transmittance at the short-wavelength region between the transmission edge and about 450 nm can be observed. Furthermore, the transmission and absorption edges are shifted to the longer wavelength (red-shifted) as the thickness of the film increased. The band gaps of the films were estimated using Tauc plots obtained from the absorption spectra. The band gap decreased from 3.49 eV to 3.34 eV as the thickness increased, as shown in Table 2. The decrease in band-gap energy is consistent with the observed red shift in the transmission and absorption edges as the thickness increased. The decrease in the band-gap energy and the red shift in the transmission and absorption edges is ascribed to the increase in defect states as the thickness of the film increased, since defect states tend to form just below the conduction band. The most common defects formed in TiO_2 are oxygen vacancies and trivalent titanium (Ti^{3+}) ions. These defects create deep electron traps that are manifested as localized states. It has been estimated that these defect states are located between 0.75 eV to 1.00 eV below the conduction-band minimum [31,32].

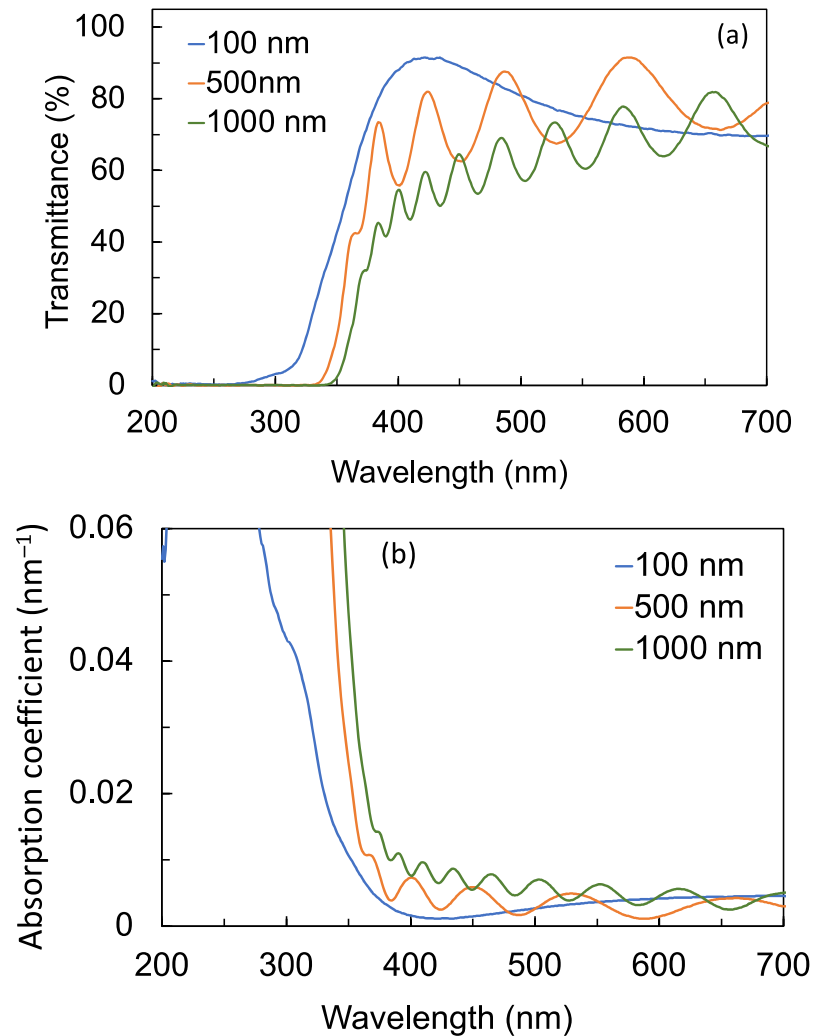


Figure 4. (a) Transmission and (b) absorption spectra of the TiO_2 films with film thicknesses of 100 nm, 500 nm, and 1000 nm. The Fabry–Perot fringes observed in the spectra are due to multiple reflections from the substrate.

Table 2. Transmission edge and band-gap energy of the TiO₂ films with 100 nm, 500 nm, and 1000 nm film thicknesses.

Thickness (nm)	Transmission Edge (nm)	Band Gap (eV)
100	320	3.49
500	335	3.44
1000	345	3.34

Figure 5a shows the current voltage (I-V) characteristics of the thin-film photoconductive detectors under 260 nm UV-C illumination, while Figure 5b shows the I-V characteristics under darkness. The photocurrent is observed to be about two orders of magnitude greater than the dark current, indicating that the TiO₂ films are photoconductive. The detector with the 100 nm film thickness exhibits a linear increase in the photocurrent as the bias voltage is increased. On the other hand, the detectors with the 500 nm and 1000 nm films exhibit a nonlinear increase in the photocurrent at low bias voltages, before eventually displaying a linear increase in the photocurrent from about 10 V bias voltage. The nonlinear increase in photocurrent implies that the mobility of photo-generated carriers is reduced. Reduced mobility is due to the presence of defects in the film. As discussed in the preceding paragraph, the number of defects increased as the thickness of the film increased. These defects also serve as trapping centers for the photo-generated carriers. Consequently, the carrier density in the detectors with 500 nm and 1000 nm films is reduced compared with the detector with the 100 nm film. This would explain the decreased photocurrent as the thickness of the film increased. At the maximum applied bias voltage of 40 V, the photocurrents from the 100 nm, 500 nm, and 1000 nm films are 8.3 nA, 5.8 nA, and 2.2 nA, respectively. For reference, the photoconductivity of just the undoped Si substrate was obtained and, at 40 V bias voltage, the photocurrent measured was 0.08 nA. This confirms that the TiO₂ films are photoconductive, while the Si substrate is not.

The photoconductivity of the TiO₂ detector can be determined from the photocurrent and the structural dimensions of the electrodes as illustrated in Figure 6 as follows:

$$\Delta i = J_{av}A \quad (4)$$

where Δi is the measured photocurrent, A is the cross-sectional area of the detector, and J_{av} is the average current density given by

$$J_{av} = \frac{J_1 + J_2 + \dots + J_n}{n} \quad (5)$$

The current density J is related to the photoconductivity (Z) and electric field (E), as $J = ZE$. The electric field is further related to the bias voltage (V_{bias}), the voltage V_2 at the input of the board, and the distance between the electrode pair (l) according to $V_{bias} - V_2 = El$. The voltage V_2 is very close to 0.7 V as the drop on the 100 ohm resistor is negligible due to the nanometric current flowing through it. The distance between the electrode pair is alternately equal to l_1 or l_2 . Therefore, the average current density can be written as

$$J_{av} = \frac{1}{2}Z \left[\frac{V_{bias} - 0.7}{l_1} + \frac{V_{bias} - 0.7}{l_2} \right] \quad (6)$$

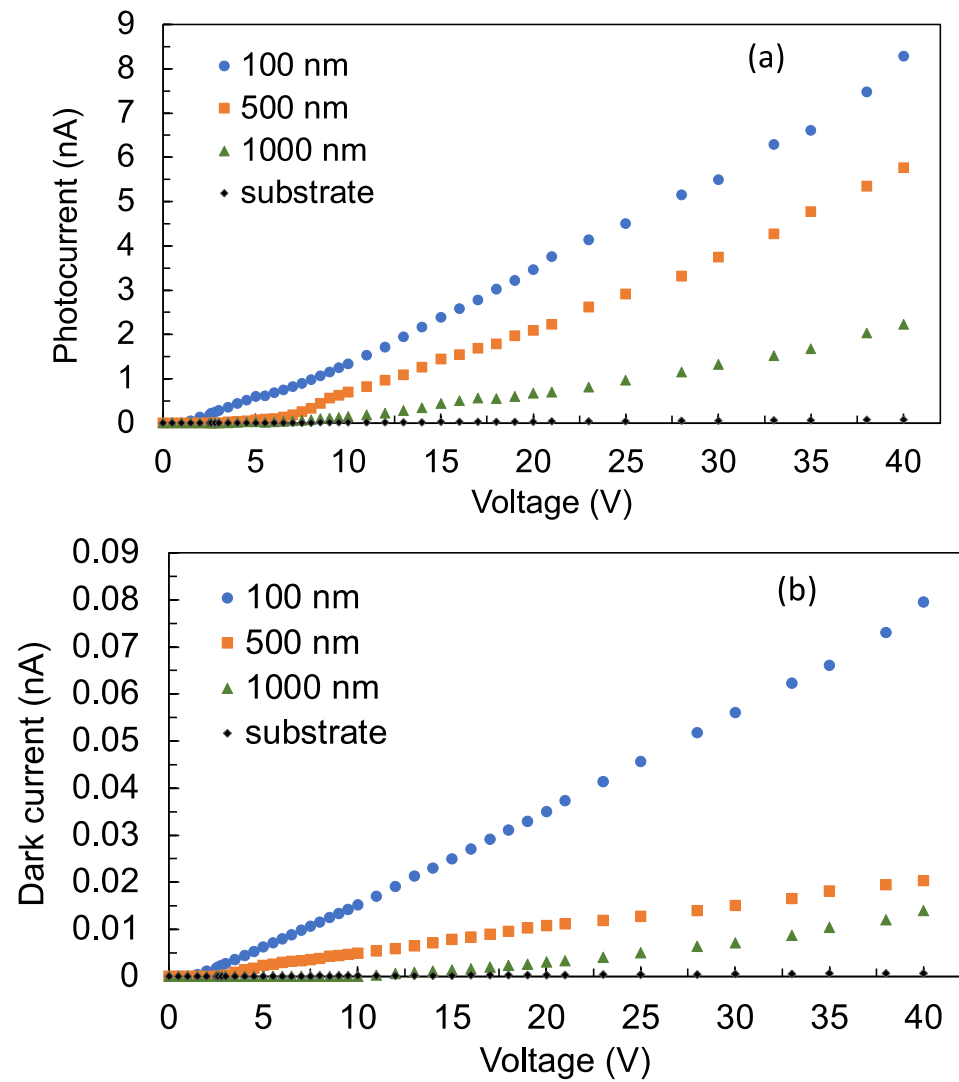


Figure 5. I-V characteristics of the detectors with 100 nm, 500 nm, and 1000 nm film thicknesses (a) under 260 nm UV-C illumination and (b) under darkness when the light source is turned off.

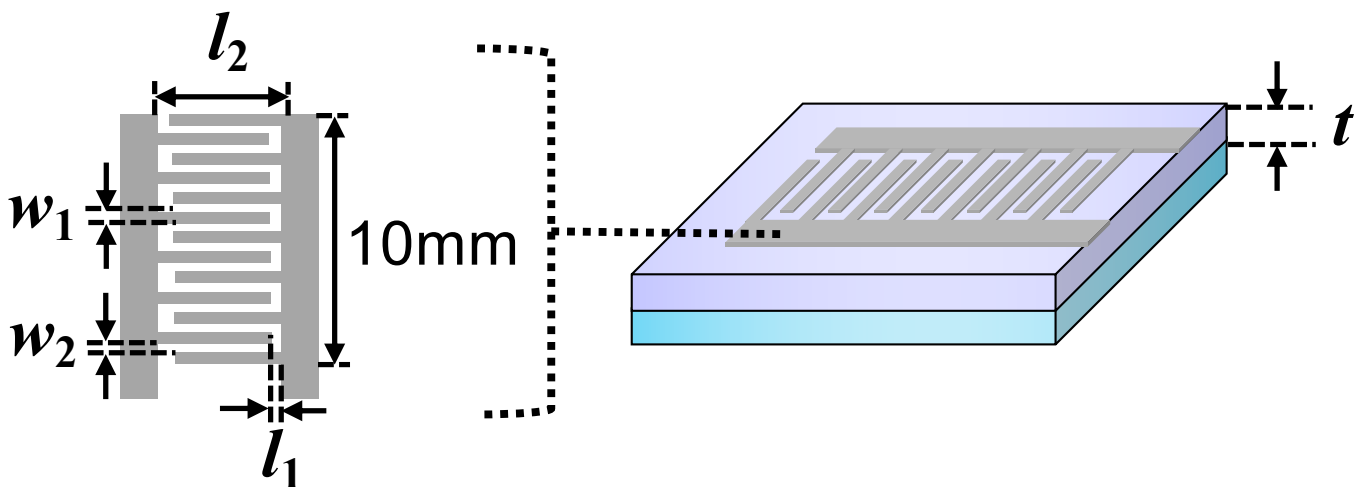


Figure 6. Dimensions of the aluminum electrode. $l_1 = 0.6$ mm, $l_2 = 4.8$ mm, $w_1 = 0.4$ mm, $w_2 = 0.4$ mm, and $n = 13$ interdigitated electrode arrays.

Assuming that current is generated only between the electrode pairs, the cross-sectional area A can be calculated from

$$A = \frac{n}{2}(tw_1) + \frac{n}{2}(tw_2) \quad (7)$$

where t is the thickness of the film, w is the width of the electrode, and n is the number of interdigitated electrode arrays. By combining Equations (5), (7) and (8), the photoconductivity is then given by

$$Z = \frac{4\Delta i}{ntV_{\text{bias}}(w_1 + w_2)\left(\frac{1}{l_1} + \frac{1}{l_2}\right)} \quad (8)$$

The photoresistance of the detector is determined according to

$$\Delta i = \frac{V_{\text{bias}} - V_2}{R_p + \Delta\text{photoresistance}} \quad (9)$$

where R_p is the 100 Ω resistance of the potentiometer and V_2 is the voltage at the detector's bottom electrode, which is about 0.7 V. Because of the very small photocurrent, the voltage drop across the 100 Ω resistor will be much less than a millivolt. Hence, $V_{\text{bias}} - 0.7$ V is equal to the electric field times the distance between the electrodes and

$$\Delta\text{photoresistance} = \frac{El}{\Delta i} - R_p \quad (10)$$

The photoconductance can be calculated as the inverse of the photoresistance. As shown in Figure 7a,b, the photoconductivity and photoconductance follow the observed trend in the photocurrent, whereby both decreased in the thicker films. In particular, the nonlinear behavior for low bias voltage, fewer than 10 V, is clearly observable.

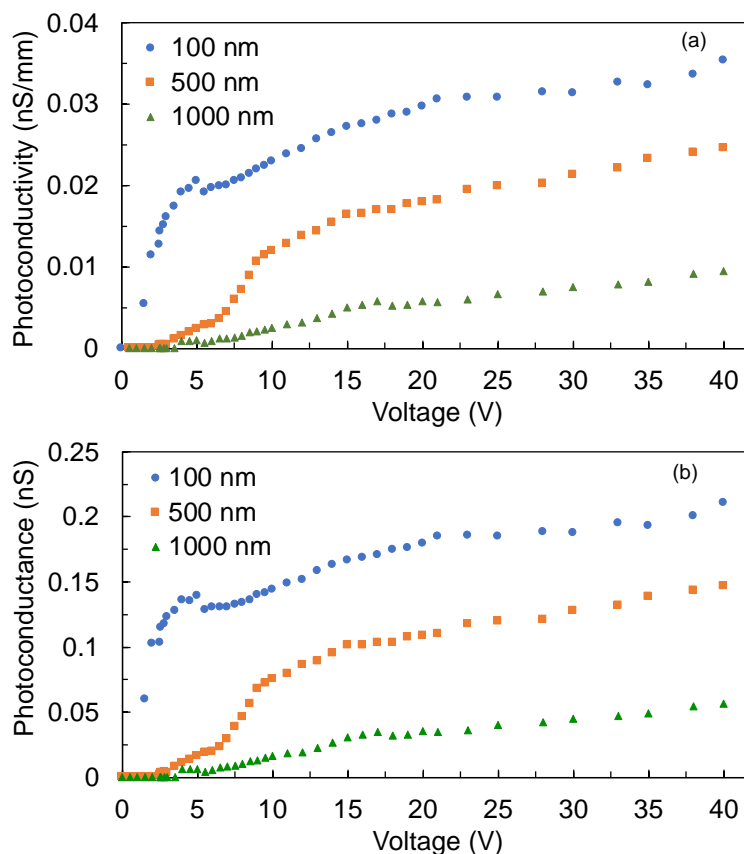


Figure 7. (a) Photoconductivity and (b) photoconductance of the detectors with 100 nm, 500 nm, and 1000 nm film thicknesses.

To further explore the nature of the defects and their role in decreasing the photocurrent, photoconductivity, and photoconductance, the photoluminescence emission from the films was evaluated when each of the films were excited by 260 nm UV-C photons. Figure 8 shows a broad luminescence from 325 nm to 450 nm. Comparing the luminescence spectra in Figure 8 with the transmission spectra in Figure 4a, the wavelength range of the broad luminescence coincides with the wavelength range where the transmittance decreased. Moreover, the luminescence intensity increased, while the transmittance decreased as the films became thicker. The luminescence emission can therefore be attributed to the radiative recombination of electrons in deep traps and holes in the valence band [30,33–38]. The increase in the luminescence intensity confirms that thicker films have more defect states. Although these defect states enhanced electron–hole recombination and therefore luminescence intensity, these defect states also served as electron traps that reduced the carrier mobility and carrier concentration, leading to the reduction in the photocurrent. These results suggest that although the 1000 nm film is more crystalline compared with the 100 nm film, as shown in Figure 3, the increased number of defects in thicker films has a more significant effect in decreasing the photoconductivity of the detector. A similar behavior was observed in ZnGa₂O₄ thin-film transistors, where the number of oxygen vacancies had a more pronounced effect on the transistor’s conductivity compared with the film’s crystallinity [37].

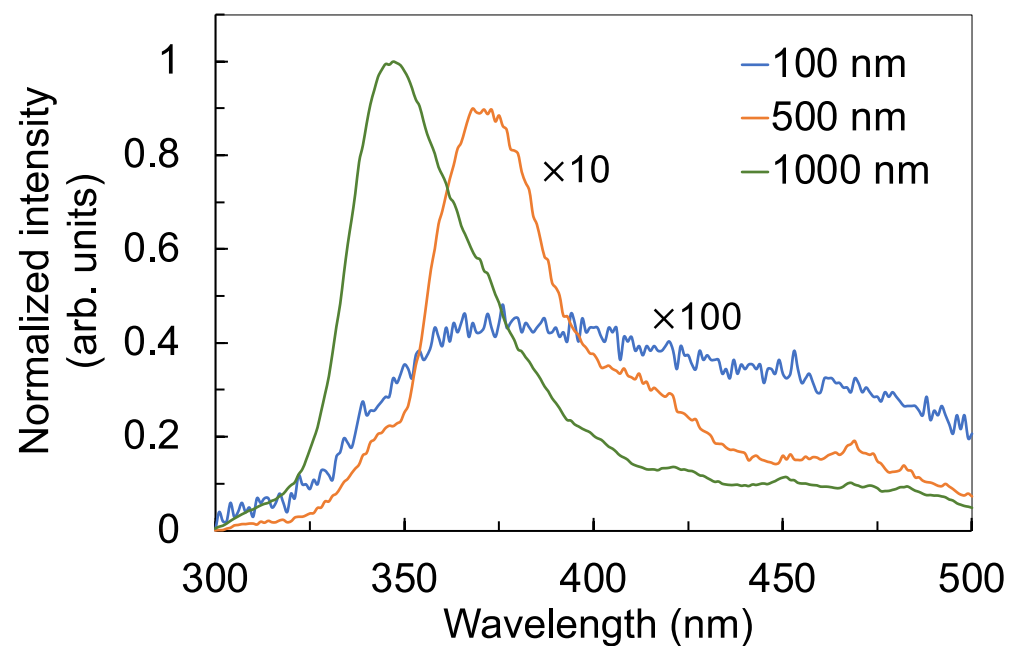


Figure 8. Photoluminescence emission spectra of the TiO₂ thin films with thicknesses of 100 nm, 500 nm, and 1000 nm under 260 nm UV-C excitation. The luminescence intensity of the 500 nm and 100 nm films were zoomed-in by a factor of 10 and 100, respectively, for ease of comparison.

Figure 9 shows the photoresponsivity (R_λ) of the detectors. The photoresponsivity was calculated using

$$R_\lambda = \frac{I_{photo}}{P_{in}} \quad (11)$$

where I_{photo} is the photocurrent and P_{in} is the power of the 260 nm UV-C light incident on the detector, which is 18.7 μ W. Since photoresponsivity is proportional to the photocurrent, the photoresponsivity of the detector also decreased as the films became thicker. At 40 V bias voltage, the photoresponsivities of the detectors with 100 nm, 500 nm, and 1000 nm film are 122.9 mA/W, 85.6 mA/W, and 33.1 mA/W, respectively. In comparison to previously reported UV-C photodetectors, the photoresponsivity of AlN film at 30 V bias voltage and 160 nm wavelength illumination is 6 mA/W [39]. The photoresponsivity of our

TiO₂ thin-film detector at 30 V bias voltage is 81.6 mA/W, 55.6 mA/W, and 19.6 mA/W for a film thickness of 100 nm, 500 nm, and 1000 nm, respectively. Previous work on TiO₂ reported a photoresponsivity of 25.6 mA/W, which was measured directly from the TiO₂ film with 253.65 nm excitation wavelength and 10 V bias voltage [40]. On the other hand, the photocurrent from our work was limited by the TIA chip. Other works reporting the photoconductivity of ZnO used longer excitation wavelengths which are in the UV-A region (315 nm to 400 nm). For instance, a photoresponsivity of 1 A/W with an excitation wavelength of 325 nm and bias voltages of 3 V [41] and 1.5 A/W with an excitation wavelength of 370 nm and bias voltage of 5 V [42] have been reported. As the excitation wavelength moves away from the band gap of the material, the photoresponsivity also tends to decrease. Therefore, the reported photoresponsivities from ZnO are higher compared with TiO₂ or AlN.

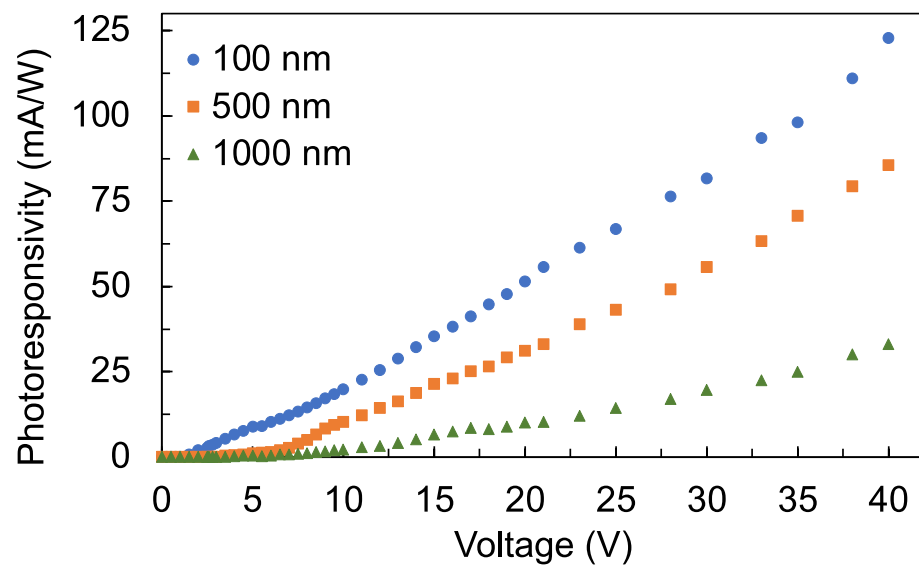


Figure 9. Photoresponsivity of the detectors with 100 nm, 500 nm, and 1000 nm film thicknesses.

The wavelength response of the TiO₂ thin-film detectors measured at a fixed bias voltage of 40 V is shown in Figure 10. The intensity of the excitation source is not flat across the wavelengths considered (200 nm to 400 nm) because the monochromator efficiency and excitation lamp emissivity changes as a function of wavelength. Therefore, the measured photocurrent was normalized by the measured power of the excitation source for each wavelength considered. The cut-off wavelengths of the detectors with 100 nm, 500 nm, and 1000 nm film thicknesses are 320 nm, 330 nm, and 345 nm, respectively. The detector will not be responsive to wavelengths that are longer than the cut-off wavelength. The cut-off wavelength of the detector is observed to shift to longer wavelengths as the thickness of the film increases. This shift is consistent with the observed red shift in the transmission and absorption edges as well as the decrease in the band-gap energy as the film becomes thicker. These results suggest that the thickness of the film may be controlled to manipulate the wavelength response of the detectors to filter out unwanted longer wavelengths, especially if the trade-off in photoconductivity is acceptable for that specific application.

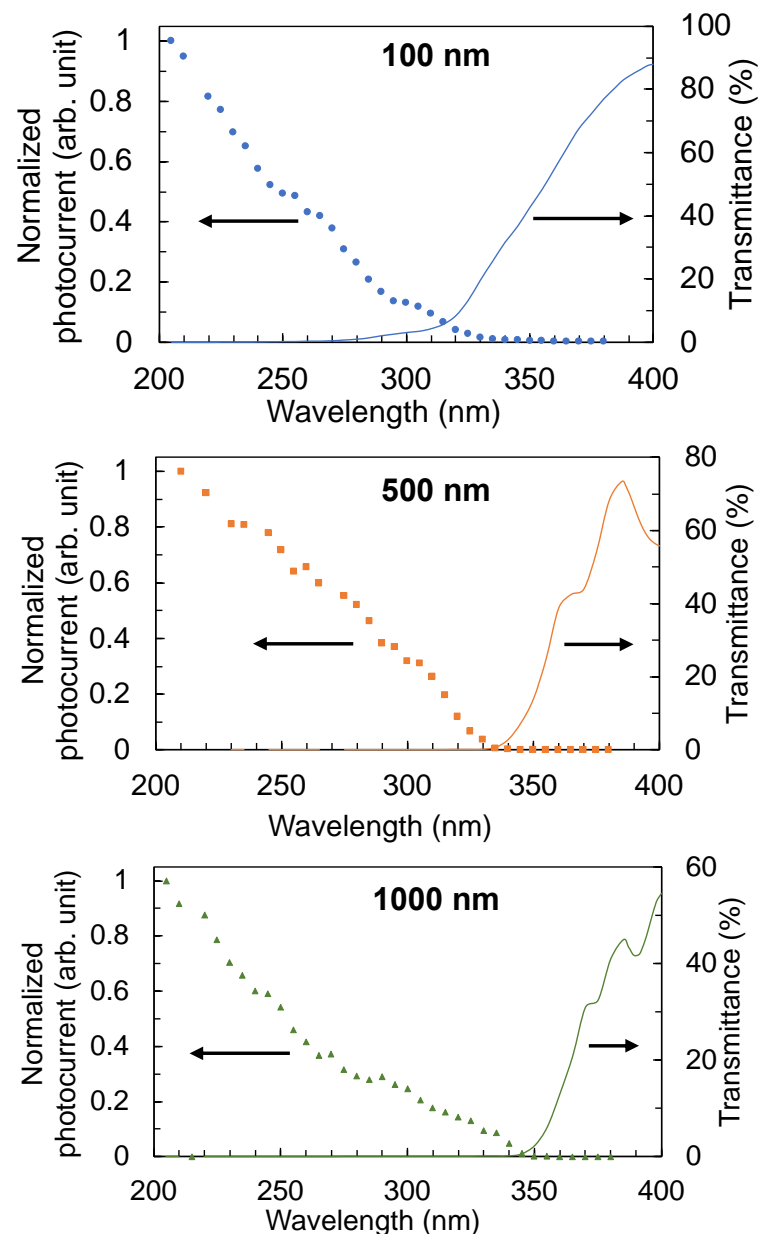


Figure 10. Wavelength response of the detectors with 100 nm, 500 nm, and 1000 nm film thicknesses. The cut-off wavelength is defined by the onset of a photocurrent being measured. The cut-off wavelength shifts to longer wavelengths as the thickness of the film increases, in accordance with the shift to longer wavelengths of the transmission and absorption edges. The photocurrents were corrected for the wavelength dependence of the excitation source.

4. Conclusions

In conclusion, the development of a photoconductive detector in the UV-C wavelength region, particularly at 260 nm, using TiO₂ thin films and a TIA, was explored. TiO₂ films of 100 nm, 500 nm, and 1000 nm thicknesses were deposited on a high-resistivity undoped Si substrate by reactive DC magnetron sputtering. The photoresponsivities of the TiO₂ thin-film detectors at 30 V bias voltage are 81.6 mA/W, 55.6 mA/W, and 19.6 mA/W for film thicknesses of 100 nm, 500 nm, and 1000 nm, respectively. These are higher than those of previously reported responsivity from AlN film, which was 6 mA/W. The effect of film thickness on the detectors' photocurrent, photoconductivity, photoconductance, photoresponsivity, and wavelength response were investigated. Interestingly, the detector which used the thinnest 100 nm TiO₂ film exhibited the best photoconductive characteristics.

Although the thicker films had better crystallinity, they also had poorer optical quality, which was manifested by the decrease in their transmittance especially around the 300 nm to 450 nm wavelength region. The lower transmittance in the thicker films can be attributed to the increased defects. The increase in the number of defects in the thicker films was also confirmed by the photoluminescence emission spectra of the films, whereby defect-related photoluminescence appeared to increase in the thicker films. The wavelength response of the detector depends on the thickness of the film as their band gap shifted to lower energy as the film thickness increased. The thickness of the film could therefore be controlled to manipulate the wavelength response of the detectors to filter out unwanted longer wavelengths. Future development of a chip-based portable UV-C detector using TiO₂ thin films will pave the way for new opportunities in a wide range of applications.

Author Contributions: Conceptualization, M.C.-R., S.M.R.H. and J.O.; methodology, M.C.-R., S.M.R.H., J.O., M.K., J.P. and J.A.H.; formal analysis, M.C.-R., S.M.R.H., J.A.H., J.P. and J.O.; investigation, M.C.-R., J.P., J.O. and M.K.; resources, M.C.-R., S.M.R.H., J.A.H. and J.O.; writing, M.C.-R. and S.M.R.H.; writing—review and editing, J.P., J.A.H. and J.O.; visualization, M.C.-R. and S.M.R.H.; supervision, S.M.R.H. and J.A.H.; project administration, M.C.-R.; funding acquisition, M.C.-R. and J.O. All authors have read and agreed to the published version of the manuscript.

Funding: This research was funded by the Catalyst: Seeding fund, provided by the New Zealand Ministry of Business, Innovation, and Employment and administered by the Royal Society Te Apārangi (CSG-MAU2003) and by the Operational Programme Research, Development and Education financed by the European Structural and Investment Funds and the Czech Ministry of Education, Youth and Sports (Project No. SOLID21-CZ.02.1.01/0.0/0.0/16_019/0000760).

Institutional Review Board Statement: Not applicable.

Informed Consent Statement: Not applicable.

Data Availability Statement: The data presented in this study are available from the corresponding author upon reasonable request.

Conflicts of Interest: The authors declare no conflict of interest. The funders had no role in the design of the study; in the collection, analyses, or interpretation of data; in the writing of the manuscript, or in the decision to publish the results.

References

1. Reed, N.G. The History of Ultraviolet Germicidal Irradiation for Air Disinfection. *Public Health Rep.* **2010**, *125*, 15–27. [[CrossRef](#)]
2. Walker, C.M.; Ko, G.P. Effect of Ultraviolet Germicidal Irradiation on Viral Aerosols. *Environ. Sci. Technol.* **2007**, *41*, 5460–5465. [[CrossRef](#)]
3. Tseng, C.C.; Li, C.S. Inactivation of viruses on surfaces by ultraviolet germicidal irradiation. *J. Occup. Environ. Hyg.* **2007**, *4*, 400–405. [[CrossRef](#)] [[PubMed](#)]
4. Kowalski, W. *Ultraviolet Germicidal Irradiation Handbook: UVGI for Air and Surface Disinfection*; Springer: Berlin/Heidelberg, Germany, 2009.
5. Adeli, B. Not If, But When: UV LED Beverage Disinfection. *IUVA News*, 6 September 2020; 10–11.
6. *The Ultraviolet Disinfection Handbook*; Bolton, J.R.; Cotton, C.A. (Eds.) American Water Works Association: Denver, CO, USA, 2008.
7. Shining a light on COVID-19. *Nat. Photonics* **2020**, *14*, 337. [[CrossRef](#)]
8. Biasin, M.; Bianco, A.; Pareschi, G.; Cavalleri, A.; Cavatorta, C.; Fenizia, C.; Galli, P.; Lessio, L.; Lualdi, M.; Tombetti, E.; et al. UV-C irradiation is highly effective in inactivating SARS-CoV-2 replication. *Sci. Rep.* **2021**, *11*, 6260. [[CrossRef](#)] [[PubMed](#)]
9. De Abajo, F.J.G.; Hernandez, R.J.; Kamminer, I.; Meyerhans, A.; Rosell-Llompart, J.; Sanchez-Elsner, T. Back to Normal: An Old Physics Route to Reduce SARS-CoV-2 Transmission in Indoor Spaces. *ACS Nano* **2020**, *14*, 7704–7713. [[CrossRef](#)]
10. Raeiszadeh, M.; Adeli, B. A Critical Review on Ultraviolet Disinfection Systems against COVID-19 Outbreak: Applicability, Validation, and Safety Considerations. *ACS Photonics* **2020**, *7*, 2941–2951. [[CrossRef](#)]
11. Jean, J.; Rodriguez-Lopez, M.I.; Jubinville, E.; Nunez-Delgado, E.; Gomez-Lopez, V.M. Potential of pulsed light technology for control of SARS-CoV-2 in hospital environments. *J. Photochem. Photobiol. B Biol.* **2021**, *215*, 112106. [[CrossRef](#)] [[PubMed](#)]
12. Ontiveros, C.C.; Shoults, D.C.; MacIsaac, S.; Rauch, K.D.; Sweeney, C.L.; Stoddart, A.K.; Gagnon, G.A. Specificity of UV-C LED disinfection efficacy for three N95 respirators. *Sci. Rep.* **2021**, *11*, 15350. [[CrossRef](#)] [[PubMed](#)]
13. Zhang, C.; Hasan, S.M. A New Floating-gate Radiation Sensor and Readout Circuit in Standard Single-Poly 130-nm CMOS Technology. *IEEE Trans. Nucl. Sci.* **2019**, *66*, 1906–1915. [[CrossRef](#)]

14. Suzuki, K.; Cadatal-Raduban, M.; Kase, M.; Ono, S. Band gap engineering of $\text{Ca}_x\text{Sr}_{1-x}\text{F}_2$ and its application as filterless vacuum ultraviolet photodetectors with controllable spectral responses. *Opt. Mater.* **2019**, *88*, 576–579. [[CrossRef](#)]
15. Yu, X.; Kato, S.; Ito, H.; Ono, S.; Kase, M.; Cadatal-Raduban, M. Filterless tunable photoconductive ultraviolet radiation detector using CeF_3 thin films grown by pulsed laser deposition. *AIP Adv.* **2020**, *10*, 045309. [[CrossRef](#)]
16. Yu, X.; Cadatal-Raduban, M.; Kato, S.; Kase, M.; Ono, S. Femtosecond PLD-grown YF_3 nanoparticle thin films as improved filterless VUV photoconductive detectors. *Nanotechnology* **2020**, *32*, 015501. [[CrossRef](#)] [[PubMed](#)]
17. Shaikh, S.K.; Inamdar, S.I.; Ganbavle, V.V.; Rajpure, Y.K. Chemical bath deposited ZnO thin film based UV photoconductive detector. *J. Alloys Compd.* **2016**, *664*, 242–249. [[CrossRef](#)]
18. Pearton, S.J.; Zopler, J.C.; Shul, R.J.; Ren, F. GaN: Processing, defects, and devices. *J. Appl. Phys.* **1999**, *86*, 1. [[CrossRef](#)]
19. Li, J.; Fan, Z.Y.; Dahal, R.; Nakarmi, M.L.; Lin, J.Y.; Jiang, H.X. 200nm deep ultraviolet photodetectors based on AlN. *Appl. Phys. Lett.* **2006**, *89*, 213510. [[CrossRef](#)]
20. Zheng, W.; Huang, F.; Zheng, R.; Wu, H. Low-dimensional structure vacuum-ultraviolet-sensitive ($\lambda < 200$ nm) Photodetector with fast-response speed based on high-quality AlN micro/nanowire. *Adv. Mater.* **2015**, *27*, 3921–3927. [[PubMed](#)]
21. Zhang, W.J.; Chong, Y.M.; Bello, I.; Lee, S.T. Nucleation, growth and characterization of cubic boron nitride (cBN) films. *J. Phys. D Appl. Phys.* **2007**, *40*, 6159. [[CrossRef](#)]
22. Samantaray, C.B.; Singh, R.N. Review of synthesis and properties of cubic boron nitride (c-BN) thin films. *Int. Mater. Rev.* **2005**, *50*, 313–344. [[CrossRef](#)]
23. Li, Y.; Guo, J.; Zheng, W.; Huang, F. Amorphous boron nitride for vacuum-ultraviolet photodetection. *Appl. Phys. Lett.* **2020**, *117*, 023504. [[CrossRef](#)]
24. Zheng, W.; Lin, R.; Zhang, Z.; Huang, F. Vacuum-ultraviolet Photodetection in few-layered h-BN. *ACS Appl. Mater. Interfaces* **2018**, *10*, 27116–27123. [[CrossRef](#)] [[PubMed](#)]
25. Watanabe, K.; Taniguchi, T.; Niiyama, T.; Miya, K.; Taniguchi, M. Far-ultraviolet plane-emission handheld device based on hexagonal boron nitride. *Nat. Photonics* **2009**, *3*, 591. [[CrossRef](#)]
26. Balducci, A.; Marinelli, M.; Milani, E.; Morgada, M.E.; Tucciarone, A.; Verona-Rinati, G.; Angelone, M.; Pillon, M. Extreme ultraviolet single-crystal diamond detectors by chemical vapor deposition. *Appl. Phys. Lett.* **2005**, *86*, 193509. [[CrossRef](#)]
27. Uchida, K.; Ishihara, H.; Nippashi, K.; Matsuoka, M.; Hayashi, K. Measurement of vacuum ultraviolet radiation with diamond photo detectors. *J. Light Vis. Eng.* **2004**, *28*, 97. [[CrossRef](#)]
28. Lin, C.-N.; Lu, Y.-J.; Yang, X.; Tian, Y.-Z.; Gao, C.-J.; Sun, J.-L.; Dong, L.; Zhong, F.; Hu, W.-D.; Shan, C.-X. Diamond-based all-carbon Photodetectors for solar-blind imaging. *Adv. Opt. Mater.* **2018**, *6*, 1800068. [[CrossRef](#)]
29. Bedikyan, L.; Zakhariyev, S.; Kejzlar, P.; Volesky, L.; Zakhariyeva, M.; Petkov, N.; Louda, P. Preparation and characterization of TiO_2 thin films for UV sensor. *MM Sci. J.* **2015**, *12*, 201520. [[CrossRef](#)]
30. Cadatal-Raduban, M.; Yamanoi, K.; Olejnicek, J.; Kohuot, M.; Kato, S.; Horiuchi, Y.; Kato, T.; Haoze, Y.; Sarukura, N.; Ono, S. Titanium dioxide thin films as vacuum ultraviolet photoconductive detectors with enhanced photoconductivity by gamma-ray irradiation. *Thin Solid Film.* **2021**, *726*, 138637. [[CrossRef](#)]
31. Zhang, M.; Zhang, H.; Lv, K.; Chen, W.; Zhou, J.; Shen, L.; Ruan, S. Ultraviolet photodetector with high internal gain enhanced by $\text{TiO}_2/\text{SrTiO}_3$ heterojunction. *Opt. Exp.* **2012**, *20*, 5936–5941. [[CrossRef](#)]
32. Mercado, C.C.; Knorr, F.J.; McHale, J.L.; Usmani, S.M.; Ichimura, A.S.; Saraf, L.V. Location of Hole and Electron Traps on Nanocrystalline Anatase TiO_2 . *J. Phys. Chem. C* **2012**, *116*, 10796–10804. [[CrossRef](#)]
33. Cadatal-Raduban, M.; Kato, T.; Horiuchi, Y.; Olejnicek, J.; Kohout, M.; Yamanoi, K.; Ono, S. Effect of substrate and thickness on the photoconductivity of nanoparticle titanium dioxide thin film vacuum ultraviolet photoconductive detector. *Nanomaterials* **2021**, *12*, 10. [[CrossRef](#)]
34. Singh, C.; Panda, E. Variation of electrical properties in thickening Al-doped ZnO films: Role of defect chemistry. *RSC Adv.* **2016**, *6*, 48910–48918. [[CrossRef](#)]
35. Tseng, Z.-L.; Kao, P.-C.; Chen, Y.-C.; Juang, Y.-D.; Kuo, Y.-M.; Chu, S.-Y. Effect of thicknesses on the structure, conductivity, and transparency of Al-doped ZnO anodes in organic light-emitting diodes. *J. Electrochem. Soc.* **2011**, *158*, J310–J315. [[CrossRef](#)]
36. Saravanan, K.; Krishnan, R.; Hsieh, S.H.; Wang, H.T.; Wang, Y.F.; Pong, W.F.; Asoka, K.; Avasthi, D.K.; Kanjilal, D. Effect of defects and film thickness on the optical properties of ZnO-Au hybrid films. *RSC Adv.* **2015**, *5*, 40813–40819. [[CrossRef](#)]
37. Cheng, L.-C.; Wu, M.-R.; Huang, C.-Y.; Juang, T.-K.; Liu, P.-L.; Horng, R.-H. Effect of defects on the properties of ZnGa_2O_4 thin-film transistors. *ACS Appl. Electron. Mater.* **2019**, *1*, 253–259. [[CrossRef](#)]
38. Kumar, N.; Patel, M.; Nguyen, T.T.; Kim, S.; Kim, J. Effect of TiO_2 layer thickness of TiO_2/NiO transparent photovoltaics. *Photovoltaics* **2021**, *29*, 943–952. [[CrossRef](#)]
39. Jia, L.; Zheng, W.; Huang, F. Vacuum-ultraviolet photodetectors. *PhotoniX* **2020**, *1*, 22. [[CrossRef](#)]
40. Xing, J.; Wei, H.; Guo, E.-J.; Yang, F. Highly sensitive fast-response UV photodetectors based on epitaxial TiO_2 films. *J. Phys. D Appl. Phys.* **2011**, *44*, 375104. [[CrossRef](#)]
41. Liu, M.; Kim, H.K. Ultraviolet detection with ultrathin ZnO epitaxial films treated with oxygen plasma. *Appl. Phys. Lett.* **2004**, *84*, 173–175. [[CrossRef](#)]
42. Liang, S.; Sheng, H.; Liu, Y.; Huo, Z.; Lu, Y.; Shen, H. ZnO Schottky ultraviolet photodetectors. *J. Cryst. Growth* **2001**, *225*, 110–113. [[CrossRef](#)]